Soft Matter

Dynamics Control of In-Plane-Switching Liquid Crystal Cell using Heterogeneous Substrates

Journal:	*Soft Matter*
Manuscript ID	SM-ART-08-2019-001742.R1
Article Type:	Paper
Date Submitted by the Author:	04-Nov-2019
Complete List of Authors:	Lee, Kuang-Wu; Kyoto University Graduate School of Science Faculty of Science Department of Physics Division of Physics and Astronomy Araki, Takeaki; Kyoto University Graduate School of Science Faculty of Science Department of Physics Division of Physics and Astronomy Yamamoto, Jun; Kyoto University Graduate School of Science Faculty of Science Department of Physics Division of Physics and Astronomy

Dynamics Control of In-Plane-Switching Liquid Crystal Cell using Heterogeneous Substrates

Kuang-Wu Lee *[a,b,c], **Takeaki Araki** [a,b] **and Jun Yamamoto** [a,b]

Received Xth XXXXXXXXXX 20XX, Accepted Xth XXXXXXXXX 20XX
First published on the web Xth XXXXXXXXXX 200X
DOI: 10.1039/b000000x

The control of surface anchoring strength can be achieved by using heterogeneous substrates. In contrast to conventional substrates that control the anchoring strength by using temperature or chemical processes, heterogeneous substrates provide surface anchoring to liquid crystal molecules by using a mixed composition of 1) a zero anchoring surface and 2) planar-anchoring patches. To study the dynamics of in-plane-switching liquid crystal displays (IPS-LCDs) under external fields, a new particle-based numerical algorithm is developed to simulate both nematic liquid crystals and heterogeneous surfaces. This new method allows us to create different heterogeneous surfaces easily by adopting predefined distributions of numerical particles. The generated effective anchoring strength from the heterogeneous surface is thus calculated, and the dynamical response is found to be similar to that of conventional homogeneously processed substrates. The results suggest that the use of a heterogeneous LCD cell is a suitable alternative for creating desirable LCD substrates, for which chemical/temperature dependences can be transferred to a more controllable configurational dependence. Interestingly, we found master curves in the peak transmittance/recovery time phase space, and they appeared to be dependent solely on the cell thickness. This discovery clarifies the fundamental optical dynamics of IPS-LCD cells.

1 Introduction

Display technologies have profoundly shaped our lives in the recent digital era. The current dominant display solution is non-emissive LCDs, which date back to the 1960s and early 1970s. By controlling liquid crystal molecules using external fields, the backlight passing through the cell can be switched ON/OFF during configurational changes of the LC directors. The reason why the LCD becomes a dominant display solution is several fold, *e.g.*, their advantages in terms of material lifetime, manufacturing cost, image resolution density, and peak brightness. On the other hand, a strong competitor in recent years is the solid-state organic light emission displays (OLEDs); they are an emissive type of display, and the comparative advantages to LCDs are obvious, such as true-black state, a fast field response, and ultra-thin structure. Therefore, in light of future development, which technology will eventually become the mainstream solution is still heavily debated[1]. LCD industries are apparently on a cusp of providing new competitive performances; otherwise, replacements would be inevitable.

Among the most recently developed LCD cells, the in-plane-switching (IPS) configuration is favored because of its wider view angle and better color reproduction[2], compared to other twist nematic liquid crystals displays (TN-LCDs). IPS cells use electrodes that are typically deployed on substrate surfaces and hence generate electric fields that are parallel to the plane. Because the electrodes and the LC long axes are on the same plane, theoretically, the viewing angle of the IPS can be as high as 178°. However, LC molecules at the interface of the IPS substrate are strongly anchored, which are typically provided by substrate treatments. These treatments create a strong anchoring that aligns the LC molecules along the surface easy axis.[3] A slow field response and relatively low peak transmittance are the major problems when comparing an IPS to other TN-LCDs. To improve IPS performances and to preserve the existing IPS advantages, it is a priority to develop a new IPS substrate that can provide both low and controllable surface anchorings.

In a search for IPS substrates that provide weak or zero anchorings, which are also called slippery surfaces, experimental attempts have been pursued via two different approaches. The first type uses a homogeneous surface in which there is polymer compound adhesion on the surface that creates a soft layer so that LC molecules at the surface are not strictly bonded to a single fixed direction[4,5]. One typically used polymer is poly(methyl methacrylate) PMMA and its anchoring force to LC molecules is controlled by temperature. Although this type of substrate indeed provides a relatively weaker anchoring, the surface easy axis is changed after every field cycle and hence

[a] *Department of Physics, Kyoto University, Kyoto, Japan*
[b] *JST CREST (Grant No. JPMJCR1424), Japan*
[c] *Friedrich-Alexander-Universität Erlangen-Nürnberg, Germany*
* *E-mail: kuangwulee@gmail.com*

makes the control of LC dynamics challenging[6]. Although it provides other potential usages, using a homogeneous polymer surface leads to easy axis rotation; hence, it is not ideal for commercial IPS applications.

On the other hand, the second approach for creating weak or zero anchorings uses a layer of polymer to mask the anchoring force from the substrate, and this treatment thus generates a near-zero azimuthal rotational viscosity[7]. One of the critical issues regarding this method is the search for materials with a low glass transition temperature (T_g) compared to room temperature, because most devices should operate in this temperature range. Due to the micro-Brownian motion of polymer chains, when the temperature is above T_g, the anchoring force to the LC molecules decreases with increasing temperature. LC cells with poly(hexylmethacrylate) (PHMA)-grafted substrates have been proposed for this use because the $T_g = -5^\circ$C of PHMA is considerably low, and it is suitable for daily use.

Energy consumption is another critical issue when using IPS-LCDs. Despite experimental attempts at producing more energy-efficient substrates, a numerical investigation was also conducted to search for new low-power consumption LCDs.[8] In that study, the authors considered bi-stable director alignments generated by conceptual heterogeneous surface configurations. Planar but orthogonal anchoring blocks were assigned alternatively on the surfaces. A Monte Carlo simulation was used to calculate the energy barriers between different configuration states. It was, therefore, a proof of concept that the LCD images can be stabilized and controlled with minimum energy consumption, which is required when only switching states.

By using similar heterogeneous configurations, we will focus on improving the IPS-LCD performances by mixing planar and slippery surfaces on the same substrate. Two performance indices are decisive for LCD cells: 1) the peak transmittance from the backlight and 2) the recovery time, which is defined as the elapsed time after the transmittance drops to e^{-1} of its peak value.

It is noted that, the field responsiveness can refer to either the field orientation time (ON) or recovery time (OFF). Because they are positively correlated, we only examine the recovery time because it involves a more straightforward determination.

In this study, a new particle-based numerical model is developed to simulate constrained nematic liquid crystals and to recreate the surface mixing of different anchoring substrates. The paper is organized as follows: We first introduce the theoretical background of our numerical model in Sec.2, including the specific setup for heterogeneous surface anchoring. The general simulated optical dynamics of heterogeneous IPS-LCDs is discussed in Sec.4.1, where the transmittance spatial variation and LC distortion dynamics are discussed in detail. In Sec.4.5 we introduce an universal master curve found in the performance indices phase space, for which it appears to depend only on the cell depth. Finally, in Sec.4.6, the comparison of a conventional IPS and the proposed heterogeneous IPS is discussed. We propose that the replacement with heterogeneous substrates results in more straightforward control of the surface anchoring strength, which paves the way for manufacturing of high-performance IPS-LCDs.

2 System description and physical model

The numerical model used in this study is established on a particle-based mesoscopic hydrodynamic algorithm, *i.e.*, stochastic rotational dynamics (SRD)[9]. It is noted that, the numerical particle does not represent a single fluid molecule in the SRD algorithm, but it is instead a mesoscopic representation that shows the coarse-grained behavior of a cluster of fluid molecules. The standard SRD procedure involves two numerical steps: 1) a free-streaming step for updating the particle positions, and 2) a particle collision step for updating the particle velocities. By executing these two steps alternatively, the fluid behaviors are generated in this algorithm. The hydrodynamic properties of the SRD model have been validated in previous studies[10]. It has been shown that the SRD algorithm successfully reconstructs Navier-Stokes behavior, and the fluid transport properties, such as shear viscosity and Green-Kubo relations, agree well with theoretical predictions. This particle-based algorithm has been applied to numerous complex fluid systems, such as the modeling of solvent dynamics in colloid[11–13] and polymer systems[14,15].

When the molecular director is further considered as an extra degree of freedom and its orientation dynamics follows the nematic interaction with neighbors, we can establish a SRD method for a liquid crystal fluid (LC-SRD). Similar to the normal SRD for isotropic fluids, an anisotropic LC-SRD particle represents the coarse-grained behavior of a LC molecule cluster. This means that the director of our numerical particle represents the average directors of a cluster of LC molecules. This approach was used in our previous studies on non-Newtonian LC shear banding[16] and the spontaneous LC electroconvection under external electric fields[17].

In the above-mentioned studies, the backflow generated by the LC configuration was calculated from the LC directors. The director-based backflow, however, is also known to be problematic if the boundary conditions are not well defined. This problem manifests, *e.g.*, when a pair of anti-parallel directors causes a large director gradient, and eventually it generates non-physical backflows owing to distortion stress. Although it is computationally stable, this ambiguity (parallel/anti-parallel) produces unreliable results. To avoid this ambiguity, an order tensor, instead of a LC director, is used to describe the backflow effect in the current nematohydrodynamic model. This tensor modification has been tested

in a recent study of the generation of optical nonlinearity in laser transient grating LC cells [18].

To study the LC rheological and orientational responses under an external field, the nematohydrodynamics model proposed by Qian and Sheng [19] was used to calculate the backflow effects. This model is based on calculating the evolution of the tensor order parameter, $\overleftrightarrow{Q}(=Q_{\alpha\beta})$, as

$$\overleftrightarrow{Q} = \frac{1}{N}\sum_{i=1}^{N}\left(\frac{3}{2}\vec{d}_i\otimes\vec{d}_i - \frac{1}{2}\overleftrightarrow{I}\right),$$

where $\vec{d}_i$ is the unit director of particle i, the coordinate indices, $[\alpha,\beta]\in[x,y,z]$, and the unit tensor, $\overleftrightarrow{I}(=\delta_{\alpha\beta})$. The order tensor is averaged over all the particles in each simulation cell, which on average contains N particles per cell.

In this nematohydrodynamic model, the development of the hydrodynamic flow, $\vec{v}$, involves several contributions, *i.e.*, from the distortion stress, $\overleftrightarrow{\sigma}^{\mathrm{d}}$, field-induced stress $\overleftrightarrow{\sigma}^{\mathrm{f}}$, and viscous stress $\overleftrightarrow{\sigma}'$ tensors. The governing equations for the cell-wise bulk flow, $\vec{v}$, in the Qian-Sheng model are as follows, [19]

$$\rho\frac{d\vec{v}}{dt} = \nabla\cdot(-p\overleftrightarrow{I} + \overleftrightarrow{\sigma}^{\mathrm{d}} + \overleftrightarrow{\sigma}^{\mathrm{f}} + \overleftrightarrow{\sigma}'), \tag{1}$$

where p is the cell-wise thermal pressure. One advantage of this model is that the represented flow fields around the topological defects have no ambiguity, whereas the director based model gives spurious results.

With one elastic constant assumption, the distortion stress tensor becomes $\overleftrightarrow{\sigma}^{\mathrm{d}} = -K(\nabla\overleftrightarrow{Q}\otimes\nabla\overleftrightarrow{Q})$, where $K(=K_1=K_2=K_3)$ is the Frank elastic constant. Here K_1, K_2 and K_3 are the elastic moduli of the spray, twist, and bend distorsions, respectively. It is noted that, one elastic constant assumption is widely used, and it is based on the fact that all three Frank elastic constants are usually of the same order, and they are typically very small ($\approx 10^{-12}$N) when an external field or bulk LC flows are present. We use this more computational compact assumption in this study, however, using different elastic constants might be necessary for pure LC rheology, such as in LC microfluidics. In the presence of an external field, the flow correction from the field-induced stress is $\nabla\cdot\overleftrightarrow{\sigma}^{\mathrm{f}} = \rho_{\mathrm{e}}\vec{E}_{\mathrm{ext}}$, where $\rho_{\mathrm{e}} = \nabla\cdot(\overleftrightarrow{\varepsilon}\cdot\vec{E}_{\mathrm{ext}})$ represents the field-induced space charge in dielectric materials. The material dielectric tensor $\overleftrightarrow{\varepsilon} = \varepsilon_{\perp}\overleftrightarrow{I} + \varepsilon_{\mathrm{a}}\overleftrightarrow{Q}$ has an anisotropic part, $\varepsilon_{\mathrm{a}} = \varepsilon_{\parallel} - \varepsilon_{\perp}$.

The viscous stress tensor in our model retains the original form, in which the Miesowicz viscosities due to different LC configurations under flow can be represented correctly. This viscous stress tensor, $\overleftrightarrow{\sigma}'(=\sigma'_{\alpha\beta})$, is given by

$$\sigma'_{\alpha\beta} = \beta_1 Q_{\alpha\beta}Q_{\mu\nu}A_{\mu\nu} + \beta_4 A_{\alpha\beta} + \beta_5 Q_{\alpha\mu}A_{\mu\beta} + \beta_6 Q_{\beta\mu}A_{\mu\alpha} + \frac{1}{2}\mu_2 N_{\alpha\beta} - \mu_1 Q_{\alpha\mu}N_{\mu\beta} + \mu_1 Q_{\beta\mu}N_{\mu\alpha},$$

where viscosity coefficients β_1, β_4, β_5, β_6, μ_1, and μ_2 are material parameters, and they can be derived from measured material parameters of $\alpha_1,\cdots,\alpha_6$. [19] The co-rotational rate of the strain tensor, $\overleftrightarrow{N} = \dot{\overleftrightarrow{Q}} - \overleftrightarrow{\Omega}\cdot\overleftrightarrow{Q}$ and the rate of the strain tensor, $\overleftrightarrow{A} = \frac{1}{2}(\nabla\vec{v} + (\nabla\vec{v})^T)$, are given as deformation intensities, where $\overleftrightarrow{\Omega} = \frac{1}{2}(\nabla\vec{v} - (\nabla\vec{v})^T)$ is the vorticity of the flow field.

For the LC-SRD particles the director, $\vec{d}_i$, of particle i is updated according to the general Ericksen-Leslie system [20] as

$$\dot{\vec{d}}_i = \overleftrightarrow{\Omega}\cdot\vec{d}_i - \frac{\lambda_2}{\lambda_1}\overleftrightarrow{A}\cdot\vec{d}_i + \frac{\vec{f}(\vec{d}_i)}{\lambda_1} + \vec{\xi}, \tag{2}$$

where $\lambda_1 = \alpha_2 - \alpha_3$ and $\lambda_2 = \alpha_5 - \alpha_6$ are the torque coupling coefficients [21] that define either the LC molecules are flow-aligning ($|\lambda_2/\lambda_1| \geq 1$) or flow-tumbling ($|\lambda_2/\lambda_1| < 1$). In the current study, we use the 5CB material parameters for our nematic LC, which is flow-aligning at room temperature, and it has a positive dielectric tensor of $\varepsilon_{\mathrm{a}} > 0$. The director expression is a simplification from the Q-tensor expression when the order parameter is locally a constant, which is a correct assumption within one simulation cell. This director expression for the LC rotation is also computationally easier, because the implied physics remain unchanged for the tensor expression [19]. Then, $\vec{\xi}$ represents the Gaussian white noise, and its magnitude is related to the fluid temperature. Because a mesoscopic timescale is longer than the microscopic molecular timescale, the equal partition assumption is applied to both the translational and rotational degrees of freedom via $\vec{\xi}$.

The molecular field, $\vec{f}(\vec{d}_i) = -\partial U_i/\partial\vec{d}_i$, in Eq. (2) is the vector derivative of a molecular potential, which has two terms under the external field as

$$U_i = -\varepsilon_{\mathrm{a}}(\vec{d}_i\cdot\vec{E}_{\mathrm{ext}})^2 - \frac{J}{\Delta s^3}\sum_{\langle i,j\rangle}(\vec{d}_i\cdot\vec{d}_j)^2 \tag{3}$$

where subscript j indexes all the particles in the neighborhood of particle i. Numerically, we count all the particles within the same simulation cell of volume Δs^3. J represents the interaction parameter among the particles.

Updating the particle directors depends on the molecular field, and the directors also feel the torques applied by the ambient shear flows, *i.e.*, the first and second terms on the right-hand side of Eq. (2).

2.1 Simulation parameters

The cell size and the time step for the SRD are set to Δs and Δt, respectively. The 3D simulation domain is $(x,y,z)\in([0,L_x\Delta s],[0,L_y\Delta s],[0,L_z\Delta s])$, which is divided into $L_xL_yL_z$ cubic cells. $(L_x,L_y,L_z) = (7,38,38)$ represents a thin slab geometry, which has been used in most of our studies. Thicker

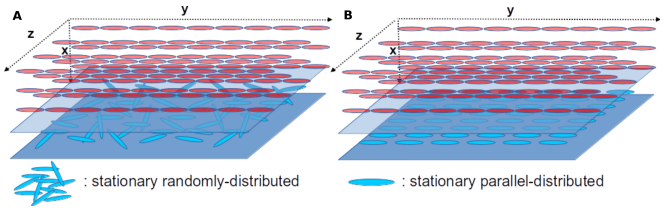

Fig. 1 Numerical models for slippery (panel A) and planar-anchoring (panel B) surfaces. The ghost particles are represented by blue ellipsoids, which are stationary and located outside the simulation domain. The nematic liquid crystal molecules are represented by red ellipsoids, which are located in the simulation domain and advance dynamically in time.

($L_x = 11$) and thinner ($L_x = 5$) slabs are also used for the transmittance dynamics comparison in which all other physical parameters are kept the same. The rotation angle for SRD collision is $\alpha = 120°$. The mass and moment of inertia for the SRD particles are m and $I = 27m\Delta s^2$, where the mass-inertial ratio of m/I represents an elongated molecular shape for nematic liquid crystals. In Eq. (3), we set $J = 0.003m(\Delta s/\Delta t)^2$,and K in the deformation stress $\overleftrightarrow{\sigma}^{\mathrm{d}}$ has the dimension of $J/(\Delta s)^3$. The initial number density of SRD particles per cell is $N = 30$, and this is used to avoid an unrealistic high thermal noise level. The particle temperature in each degree of freedom is set to: $T_x = T_y = T_z = 0.2J$, and the Boltzmann constant of $k_{\mathrm{B}} = 1$ is used in the simulations. The kinetic viscosity in our SRD simulation is given by[22]

$$\nu_{\mathrm{SRD}} = \frac{T\Delta t}{2m}\left[\frac{1}{(1-1/N)\sin^2\alpha} - 1\right] + \frac{(\Delta s)^2}{12\Delta t}. \qquad (4)$$

Other LC material parameters, $\alpha_1, \cdots, \alpha_6$ in SI units are adopted from the experimental measurements of 5CB at room temperature[24], and their relative numerical values for use in simulations are obtained by assuming $\nu_{\mathrm{SRD}} = \alpha_4/(m/\Delta s^3)$.

Periodic boundary conditions are implemented in the y and z directions. No-slip boundaries for the LC-SRD particles are used on the cell walls in the x direction. For the anchoring condition, as shown in Fig. 1, stationary ghost particles are placed outside the simulation domain (in the non-slip walls) to generate a slippery background (panel A) and planar-anchoring patches (panel B). It is noted here, we assign the planar-anchoring direction only along y in this study (excepting the calculations of extrapolation length, where a twisted anchoring cell is used). The LC anchoring strength is represented by the interaction potential between the LC and ghost particles and the distribution of their orientations. The interaction strength is given by $W_{\mathrm{anchor}}J$. Thus, W_{anchor} is the ratio of the interaction strengths between LC-ghost pairs, and LC-LC pairs. The anchoring force generated by orderly aligned ghost particles (panel B) is strong in a single direction. Its anchoring strength is controlled only by changing $W_{\mathrm{anchor}}J$. In panel A,

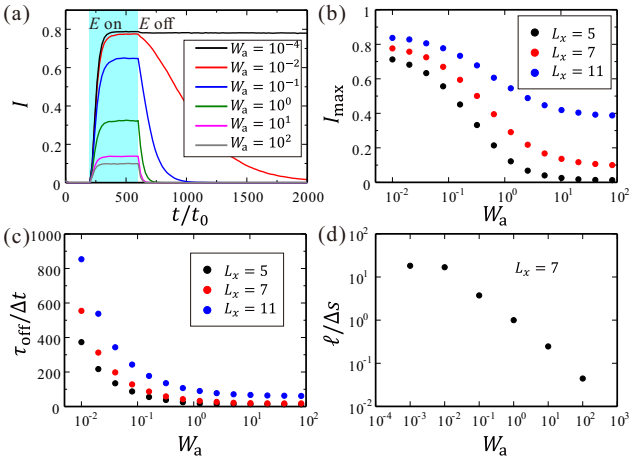

Fig. 2 (a) Performance curves for uniform planar anchoring substrates for an anchoring strength of $W_{\mathrm{anchor}} = 1 \times 10^{-4} \sim 1 \times 10^2$. The substrate type used in this simulation involved parallel-distributed ghost particles, as shown in panel B in Fig. 1. (b) Plot of the peak transmittance, $I_{\max}$, at $t = 600\Delta t$ as a function of the cell thickness L_x. (c) Plot of the recovery time, τ_{off}, against the anchoring strength, W_{anchor}, in a cell with $L_x = 7$. (d) The extrapolation length, ℓ, against the anchoring strength in a twisted anchoring cell of $L_x = 7$.

however, there is no preferential anchoring direction because the randomly distributed ghost particle do not provide a potential minimum on the surface. Thus, the anchoring strength for the azimuthal angle of the director field effectively vanishes on panel A, regardless of the value of $W_{\mathrm{anchor}}J$.

This treatment mimics the microscopic nature of potential interactions between particles. The substrate heterogeneity is generated via using these two boundaries together on the same surface, at different sites. Two types of heterogeneous substrates will be studied, *i.e.*, a slippery background with planar patches (Type I) and a planar background with slippery patches (Type II). Most of our study focus on Type I, and we use Type II for performance comparisons.

Additionally, we set the anisotropy of the dielectric constant to $\varepsilon_{\mathrm{a}} = 8\varepsilon_0$ with ε_0 being the dielectric constant of vacuum. With $\varepsilon_{\mathrm{a}} = 8\varepsilon_0$, the critical field strength for the Fréedericksz transition is numerically given by $E_{\mathrm{c}} \cong 27\sqrt{J/\varepsilon_0\Delta s^3}$. It is estimated in a uniform cell (panel B) with $W_{\mathrm{anchor}} = 1$ and $L_x = 7$. Here, the electric field is applied along the z-axis to estimate E_{c}.

2.2 Experimental setups

In the following simulations, in-plane external fields are applied as follows. Initially, an external field, $\vec{E}_{\mathrm{ext}}$, is applied along the y-axis from $t = 0$ to $t = 200\Delta t$ to align the LC director. From $t = 200\Delta t$ to $600\Delta t$, the orientation of the exter-

nal field is changed to be along the $(0, 1/\sqrt{2}, 1/\sqrt{2})$ direction, whose azimuthal angle referring to the y-axis is $\theta_E = \pi/4$. Thus, for a crossed polarizer (along y on the top) / analyzer (along z on the bottom) pair, the highest transmittance is obtained when the LCs align to $\vec{E}_{ext}$. The applied field strength is $|\vec{E}_{ext}| = 20\sqrt{J/\varepsilon_0 \Delta s^3}$. This field strength is slightly weaker than the critical strength for the Fréedericksz transition ($E_c \approx 27\sqrt{J/\varepsilon_0 \Delta s^3}$), which is defined for $\theta_E = \pi/2$. After $t = 600\Delta t$, the external field is then switched off.

The dynamics of the LC director is monitored with the temporal changes of transmittance I. It is calculated with the normalized energy flux of an incidence field as

$$I = \frac{4}{L_x} \sum_{n=0}^{L_x - 1} [\cos\theta(n) \sin\theta(n)]^2. \quad (5)$$

Here $\theta(n)$ is the in-plane angle of the director field that refers to the y-axis at the n-th plane. It is obtained with the Eigenvector of $\overleftrightarrow{Q}$, which is spatially averaged in the n-th plane. When the director field is aligned along the external field, *i.e.*, $\theta(n) \approx \theta_E$, in the whole cell, transmittance I is near unity. Because the transmittance is expected to be largest at $t = 600\Delta t$, we defined the peak transmittance to be $I_{max} = I(t = 600\Delta t)$. Additionally, we defined the recovery time after the field is switched off, τ_{off}, by solving $I(\tau_{off} + 600\Delta t) = I_{max} e^{-1}$.

3 Anchoring behaviors on uniform anchoring substrates

First, we consider the anchoring behaviors on uniform anchoring substrates. For a conventional IPS cell, a uniform planar-anchoring substrate is typically used to create on-off (bright-dark) states under an external field. Therefore we use it as a comparison reference. The physical parameters for the LC properties and the cell geometries are kept the same as those used in the later heterogeneous substrates studies. An LC is sandwiched by two parallel plates, which consist of panel B for the whole area. For the dynamic of LCs in uniform planar-anchoring substrates, the anchoring strength, W_{anchor}, is the decisive physical quantity that depends on both surface treatment and the system temperature. The complex chemical/engineering process for production is not within the scope of discussion here, but the surface anchoring strength is simply treated as a physical parameter. The simulation results for different anchoring strengths are shown in Fig. 2.

In Fig. 2(a), the temporal change of the transmittance for different values of the anchoring strength are plotted. The transmittance increases under an external field along $\theta_E = \pi/4$, and it decays to zero after the field is turned off if $W_{anchor} \geq 1 \times 10^{-2}$. As shown in Fig. 2(a), peak transmittance I_{max} decreases with increasing surface anchoring strength. The anchoring strength also controlled the recovery time, τ_{off}, after the field removal. A stronger anchoring provides a faster recovery. However we also noticed that if the anchoring strength is minimal at $W_{anchor} = 1 \times 10^{-4}$, the LC directors do not relax back to the original position, even after switching off the external field for a long time.

In Fig. 2(b), we show the peak transmittance, I_{max}, as a function of the anchoring strength, W_{anchor}, for different cell thicknesses. The peak transmittance increases with decreasing W_{anchor}. When the anchoring strength decreases, the director on the surface could deviate from the easy axis, which is along the y-axis here. Then, the total transmittance increases for smaller W_{anchor}. Because the elastic deformation of the director field is suppressed in thinner cells, the peak transmittance is decreases in the thinner cells.

In Fig. 2(c), we show the recovery time, τ_{off}, as a function of W_{anchor}. As the anchoring strength decreases, the recovery time increases considerably. For most applications of LCDs, a large peak transmittance and short recovery time are preferred; thus, there is a trade-off relationship between them when we change the anchoring strength on uniform surfaces. As described above, the director field on the surfaces deviates from the easy axis when W_{anchor} is small. This causes a weak recovering force after the field is removed and a resulting long recovery time. When $W_{anchor} < 1$, in particular, the relaxation process at the director on the substrates is more dominant than the relaxation of the elastic deformation in the bulk. Here, we confirmed that the recovery time is proportional to the square of the cell thickness, *i.e.* $\tau_{off} \propto L_x^2$, when $W_{anchor} \geq 1$ (not shown here.) For example, we obtained $\tau_{off}(L_x = 5) = 19.8\Delta t$, $\tau_{off}(L_x = 7) = 33.7\Delta t$, and $\tau_{off}(L_x = 11) = 69.4\Delta t$. The increase in the transmittance in the thick cell is due to the elastic deformation in the bulk, not the surface director, when $W_{anchor} \geq 1$.

In Fig. 2(d), we show the extrapolation length, ℓ, as a function of the anchoring strength W_{anchor} to compare our anchoring strength with those in other systems. Our extrapolation length is estimated in a twisted cell in which the uniform, but crossed anchoring directions at the top (along z) and bottom (along y) substrates are used. In a twisted cell, the director field rotates along the x axis even without the external field. The rotational rate is estimated from $\pm(\pi/2)/(L_x \Delta s + 2\ell)$, from which the extrapolation length, ℓ, is estimated for different W_{anchor}. The elastic theory predicts $\ell \propto K_2/W$, where K_2 is the elastic modulus for the twist mode, and W is the anchoring strength. In our simulations, ℓ increased with decreasing W_{anchor}; However, its dependence slightly deviates from the theoretical argument. For $W_{anchor} = 1$, the extrapolation length is similar to Δs; thus, the cell thickness of $L_x = 7$ corresponds to $L_x \Delta s \approx 7K_2/W$ in actual systems.

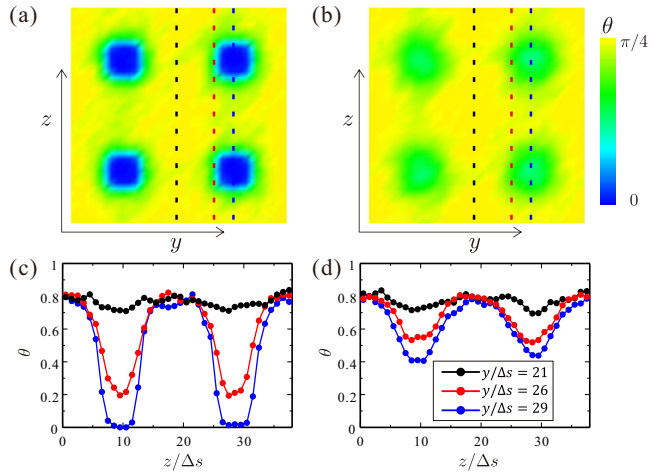

Fig. 3 Distortion of the LC directors under an external field at (a) the substrate surface and (b) in the cell mid-plane. The heterogeneous substrates used have four evenly-distributed patches. The colorbars indicate the angles of the LC directors on the yz plane, referring to the y-axis. The angle profiles along certain lines are plotted at (c) the substrate (c) and (d) mid-plane.

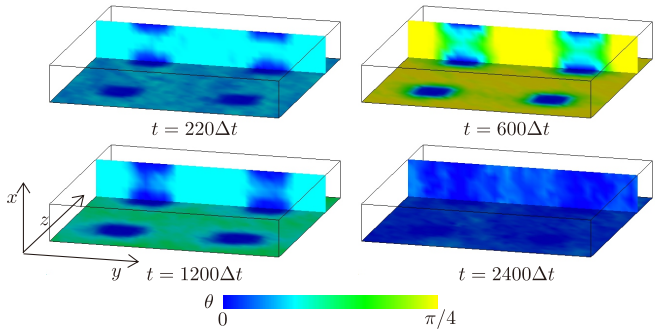

Fig. 4 3D director evolution in a heterogeneous LCD cell, with $A_{\text{patch}} = 3.48\%$ for four patches. An external $\theta_{\text{E}} = \pi/4$ electric field, referring to y-axis, is applied from $t = 200\Delta t$ to $600\Delta t$.

4 Anchoring behaviors on heterogeneous substrates

4.1 General optical dynamics

Next we consider the anchoring behaviors on heterogeneous substrates composed of panel A and B. We define the surface fraction value as $A_{\text{patch}} = S_{\text{patch}}/(S_{\text{slip}} + S_{\text{patch}})$, where S_{patch} and S_{slip} are the area sizes of the patched and slippery sites, respectively. We assign the circular patches to have planar anchoring along the y-axis, and the slippery background allows the LC directors to rotate freely on the surface (Type I). The interaction strength between the LC particles and the ghost particles is set to $W_{\text{anchor}} = 1$.

The LC director distortions in the heterogeneous LCD cell, under the same external electric field of $\theta_{\text{E}} = \pi/4$, is demonstrated in Fig. 3. The maps of the in-plane director angle are shown in the upper panels on the substrate surface in Fig. 3(a) and in the cell mid-plane in Fig. 3(b). The results shown are for a substrate pair with 2×2 planar patches, on which the patch radii are set to $r = 2\Delta s$, and they are evenly distributed. The angle profiles along $y/\Delta s = 21, 26, 29$ lines are shown in Figs. 3(c) and (d), respectively. On the surface plane, the LC directors align toward the external field in-between the planar patches, for which the LC angles of $\theta \approx \pi/4$ are shown in yellow. However, the LC directors align toward the y-axis so their angles, $\theta \to 0$, are due to the strong anchoring from the planar patches. As shown in Figs. 3(b) and (d), this anchoring effect is less pronounced in the cell mid-plane. Compared to the substrate surface, the LC distortions in the cell mid-plane near the patch sites are thus more influenced by the external field; thus, so the angle increases to $\theta \approx 0.4$ (as shown in Fig. 3(d).)

Although the LC distortion shows a cell-height dependence, the different temporal evolutions of the LC distortion at different yz positions result in a non-uniform transmittance distribution. In Fig. 4, 3D temporal structures of LC distortion are shown: near the beginning of external field application ($t = 220\Delta t$), right before the field switching-off ($t = 600\Delta t$), in the middle of recovery ($t = 1200\Delta t$), and when the directors finally returned to the initial equilibrium ($t = 2400\Delta t$). As shown if a point in the cell is away from the planar patches, the LC distortions are more determined by the external field, rather than controlled by the patch anchoring. The LC distortions at those points clearly show distinct dynamics from those LC molecules that were directly sandwiched between the planar patches.

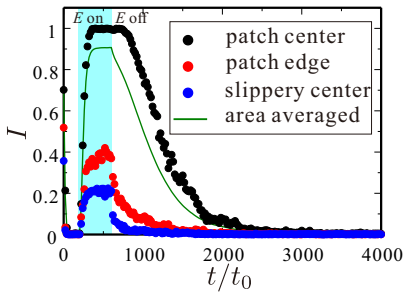

Fig. 5 Performance curves for the heterogeneous substrates, with $A_{\text{patch}} = 3.48\%$. The solid green line shows the area-averaged profile, whereas the blue, red, and black dotted lines show the results from the patch center, patch edge, and the slippery center.

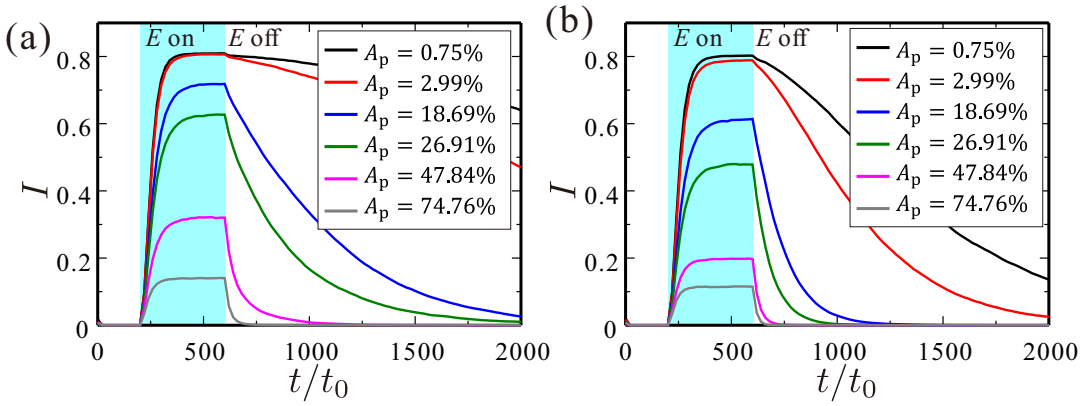

Fig. 6 Performance curves a function of the area fraction of 1 central in (a) and four planar-anchoring patches in (b). The $\theta_E = \pi/4$ field is switched on at $t = 200\Delta t$ and then switched off at $t = 600\Delta t$. For the these results, the area fractions are the same for both substrates, but the distributions of the planar-anchoring patches are different.

4.2 Spatial dependent dynamics

A direct optical observable of the heterogeneous LCD cell is the transmittance of the light incidence, for which its inhomogeneity can be observed under a microscope. The simulated transmittance inhomogeneity is shown in Fig. 5, where the transmittance evolution curves are plotted for the patch center, patch edge, and the slippery center. The area-averaged transmittance is also shown there. This area-averaged curve is typicaly considered as the transmittance observed by the human eye, although the transmittance is indeed very spatially dependent at different locations in the cell. Here, the spatial dependence of the transmittance curves are expected to also have material and temperature dependencies. This is because the LC phase transition speeds, *i.e.*, the speed of LC nematic phase propagating toward isotropic phase, either along or perpendicular to the LC director, are actually different[25].

As previously mentioned, a high transmittance under an external field and fast recovery back to equilibrium are preferred for industrial applications, and several factors can change the LCD performance curves. We thus study the performance curves under different patch configurations as discussed below.

4.3 Patch distribution effect

Patch distribution on the substrate involves difficulties during the cell preparation process, and as observed previously, the distribution configurations will also determine the spatially-dependent dynamics. We study here the performance curves for different heterogeneous configurations while maintaining the area fraction also as a controlling factor. The simulation results of one central patch and four evenly-distributed patches are shown in Figs. 6(a) and (b), respectively.

We found that by increasing the planar patch coverage (higher area fractions), the transmittance is highly decreased. This effect is due to the anchoring from the planar patches. However, we also noticed that the transmittance reduction is much more severe for the four patches (Fig. 6(b)) compared to the case of only one patch (Fig. 6(a)). This indicates that the more evenly distributed patches could provide a stronger anchoring effect. In addition to the smaller transmittance when increasing the patch area fraction, the recovery time required for returning the initial equilibrium is also shorter. These results suggest that the anchoring strength can be adjusted by merely changing the heterogeneous substrate configurations. The possibility of replacing a conventional chemical preparation for substrate anchoring will be discussed in Sec. 4.6.

Another essential issue to resolve when designing heterogeneous substrates involves the choice of patch type, *i.e.*, does the configuration of a planar patch on a slippery substrate (Type I) perform better? Or should it be *vice versa, i.e.*, slippery patch on a planar substrate (Type II), to achieve a higher performance? Despite the difficulties, when producing different substrate types, we numerically study their performances by switching the surface characteristics.

4.4 Comparison between patch types

Our performance comparison between these two types is shown in Fig. 7 in which the performance indices (the peak transmittance and recovery time) are plotted as a function of the area fractions. The left panels (Figs. 7(a) and (c)) show the results for the Type I substrates, and the right panels (Figs. 7(b) and (d)) show the results for the Type II substrates. The performances of the different patch distributions (single, 4, 9, 25, and homogeneous patches) are plotted. The homogeneous patch distribution indicates a large number of

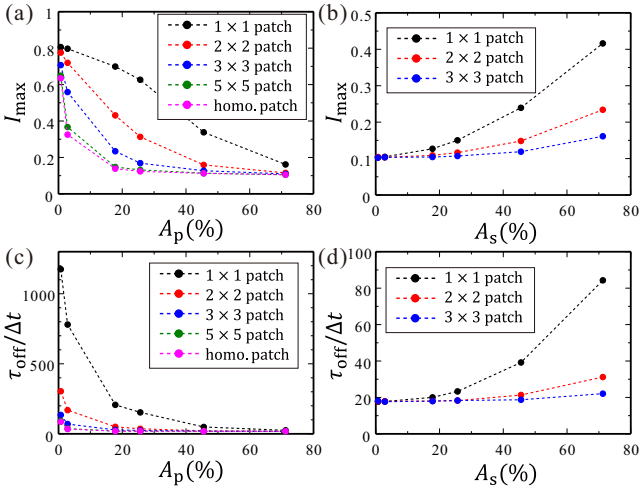

Fig. 7 Comparison of the peak transmittance, I_{max}, in (a) and (b) and the recovery time, τ_{off}, in (c) and (d) as a function of the area fraction between the Type I (planar patch) in the left panels and the Type II (slippery patch) in the right panels.

infinitesimal patches randomly attached to the substrate.

First, we focus on the Type I substrate. We observed that regardless of the patch distributions, the peak transmittance, I_{max}, and recovery time, τ_{off}, reduce when the patch area fraction is increased. This tendency is simply due to the higher anchoring strength as discussed previously. In addition, we also quickly determined the same reduction in the peak transmittance/recovery time occurs when the number of patches increases. This clearly suggests that effective anchoring becomes stronger, when finer and a larger number of patches are used. Additionally, this peak transmittance/recovery time reduction effect reaches an asymptotic value when the finer patches are used. Not shown in this figure, we also simulated the dynamics of 49 and 100 patches for the Type I substrate, and their performance indices fall in the narrow gaps between the results of the 25 patches and the homogeneous patch. Because a higher transmittance with fast recovery are favored for LCD applications, this numerical result indicates a better design when using planar patches, is to use a more distributed configuration with lower patch area fraction.

By switching to the slippery patches on the planar-anchoring surface, we also study the performances of the Type II substrates. The simulation results are shown in the right panels of Fig. 7. In contrast to the Type I substrate, the increase in the patch area fraction increases the peak transmittance/recovery time, although using finer and more patches still reduce these two indices as with the Type I substrate. Therefore, we conclude that when using the Type II substrate, the more distributed configuration is still desirable for its fast recovery; however a higher area fraction of slippery patches should be prepared.

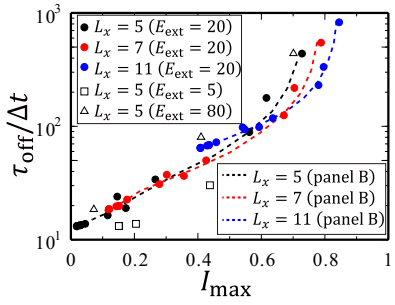

Fig. 8 Master curves in the peak transmittance/recovery time phase space are found for different cell thickness.

One interesting effect is revealed in the comparison, *i.e.*, the performance indices for the Type I and Type II are almost complementary to each other. For example, the the peak transmittance/recovery time for Type I with $A_{patch,I} = 74.76\%$ correspond almost perfectly to that for Type II with $A_{patch,II} = 26.91\%$. The results for other area fractions show similar tendency, if this condition is satisfied:

$$A_{patch,I} + A_{patch,II} \approx 100\% \quad (6)$$

According to these complementary results, the more evenly distributed patches (higher patch number) is equivalent to a more fractalized substrate background. This is the reason why the more fragmented planar-patch shares the same effect with the more fragmented slippery-patch.

4.5 Depth dependent master curves

From a practical viewpoint, it is important to determine the most decisive variables that can help easily determine the LCD designs. The performance indices, the peak transmittance and recovery time, are chosen as phase space axes, and we plot the simulation results as a function of them. We also show the I_{max}-τ_{off} curves for the uniform planar anchorings using broken lines, which are obtained in Sec. 3. For uniform planar cell the results are generated by changing the anchoring strength W_{anchor}. Surprisingly, a monotonic curve is found in the chosen phase space. This result is shown in Fig. 8 and the determined curve is called the master curve.

It is noted here, this master curve includes all the simulation results of different patch distributions, patch area fractions and even the results for uniform planar-anchoring substrates. Regardless of the different influences from those variables, the simulation results all fall on the same curve. Because the external field strength is also a factor that can change the optical performance, stronger/weaker external fields are also tested to check if the results would deviate from this master curve.

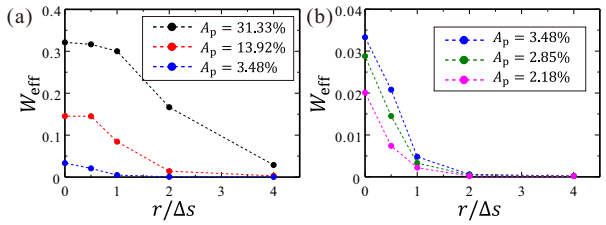

Fig. 9 Effective anchoring strength, W_{eff}, as a function of the patch radius, r, where the area fractions of the planar patch are fixed for certain values.

Surprisingly, even with different external field strengths, the results fall on the same master curve. This indicates that a higher transmittance always corresponds to slower recovery. And *vice versa*, a lower transmittance always accompanies a faster recovery (as shown in Fig. 8 for smaller $\vec{E}_{\text{small}} = \vec{E}_{\text{ext}}/4$ and larger $\vec{E}_{\text{large}} = 4\vec{E}_{\text{ext}}$) compared to the standard $\vec{E}_{\text{ext}}$ used elsewhere in this study. The master curves are clearly more pronounced, however, only in the higher transmittance/recovery region, whereas the system intrinsic thermal noise influences the measurements and exhibits strong fluctuations in lower transmittance/recovery region, as shown in the semi-log presentation.

The substrate anchoring strength and cell height are decisive for the Fréedericksz transition; therefore, the cell depth may influence the LCD performance and generate a different master curve. To verify if this master curve depends on the cell height, different heights are also considered to determine if there are also other master curves. This speculation is verified when their performance indices are plotted on the same figure. As shown in Fig. 8, thicker ($L_x = 11$) and thinner cells ($L_x = 5$) generate different master curves shifted to different sides, comparing to the standard cell ($L_x = 7$).

One thing to notice here is that, the thicker cell ($L_x = 11$) has a higher transmittance than the thinner cell ($L_x = 5$). This is because a higher peak transmittance means that the LC directors are more aligned toward the external field, which is true for the thicker cell because its large cell depth produces less alignment force to LC in the cell mid-plane. Assuming the light is not absorbed too much when passing through the LCD cell, the better field alignment is the reason why a thicker cell ($L_x = 11$) obtains a higher peak transmittance, and the less field-aligned thinner cell has a lower transmittance.

4.6 Tunable anchoring strength

The transmittance dynamics have been already determined for a constant cell height. We can immediately question if this conclusion also applies to a homogeneous planar substrate. This extrapolation of physical interpretation is positively confirmed by our simulations. In Fig. 9, the performance analogy between a heterogeneous cell and homogeneous planar cell is demonstrated.

The effective anchoring, W_{eff}, is calculated as follows. Simulations of the uniform planar substrates are performed for a wide range of anchoring strengths (see Fig. 2). When a pair of peak transmittance/recovery time indices corresponds well to the results of a heterogeneous cell, the effective anchoring strength is thus determined. This effective anchoring can be used to be pursued by complex chemical/manufacturing processes; however, the desired anchoring strength does not fall in the practical temperature range most of the time. Our simulations imply that the effective anchoring strength in the limit of a small patch size, r, is determined by the patch area fraction simply as

$$\lim_{r\to 0} W_{\text{eff}} = W_{\text{anchor}} A_{\text{patch}}. \tag{7}$$

Additionally the simulations suggest that conventional processes can be replaced by using heterogeneous substrates, which could be controlled in a much easier and precise manner.

5 Conclusions

We studied a new type of in-plane-switching liquid crystal cell that uses a heterogeneous substrate configuration. A new particle-based nematohydrodynamics model is also developed for reconstructing this special combination of surface characteristics. The heterogeneous substrates demonstrate controllable surface anchoring strength that can be easily adjusted by arranging the surface compositions. The two important performance indices, the peak transmittance and recovery time, can be considerably improved because of the reduction of the LC azimuthal anchoring at the surface. On the other hand, depth-dependent master curves are found and they represent the characteristic optical performance of each IPS-LCD cells. This finding indicated the need for using different cell heights to achieve a certain performance point that is not located on this particular master curve.

In this study, we showed our results in dimensionless units. However, it is straightforward to relate our simulation system to experimental systems. For example, we considered a nematic liquid crystal, which has an elastic modulus of $K = 10\,\text{pN}$, a rotational viscosity of $\lambda_1 = 10^{-2}\,\text{Pa}\cdot\text{sec}$, and a dielectric anisotropy of $\varepsilon_a = 8$ that is confined in a cell of $d = 3.5\,\mu\text{m}$. Its threshold external field for the Fréedericksz transition is estimated to be $E_c = \pi\sqrt{K/\varepsilon_a\varepsilon_0}/d = 3.5\times 10^5\,\text{V/m}$ and the relaxation time is $\tau_{\text{off}} = \lambda_1 d^2/\pi^2 K = 1.2\,\text{msec}$. On the other hand, our numerical system of $L_x = 7$ produced $\tau_{\text{off}} = 33.7\Delta t$ and $E_c = 27\sqrt{J/\varepsilon_0\Delta s^3}$ in our simulation units. Then, we could relate the unit length and time to $\Delta s = 0.5\,\mu\text{m}$

and $\Delta t = 37\,\mu$sec, respectively. The numerical in-plane field strength of $E_{\rm ext} = 20\sqrt{J/\varepsilon_0 \Delta s^3}$ is estimated as $E_{\rm ext} = 2.5 \times 10^5\,{\rm V/m}$, and a substrate showing $W_{\rm eff} = 0.1$ corresponds to an actual anchoring strength of $0.1K/\Delta s = 2 \times 10^{-6}\,{\rm J/m^2}$.

Regarding the advantages of using heterogeneous substrates in IPS cells, the conventional chemical treatment process is complicated, and often, very different surface materials are required to achieve a slight anchoring strength change. However, by using heterogeneous cells, one can simply modify the surface area or the patch distribution structures, and the effective anchoring strength can be adjusted to specific demands. This approach opens the door to generating high-performance LCD cells for future applications.

Acknowledgment

The authors acknowledge the support from project JST CREST Grants No. JPMJCR1424. T.A. also acknowledges the support from JSPS KAKENHI Grants No. JP17K05612.

References

1 H.-W. Chen, J.-H. Lee, B.-Y. Lin, S. Chen and S.-T. Wu, *Light Sci. Apple.*, 7, 17168 (2018)
2 M. Oh-e and K. Kondo, *Appl. Phys. Lett.*, 67, 3895 (1995)
3 M. Oh-e and K. Kondo, *Appl. Phys. Lett.*, 69, 623 (1996)
4 M. Tokita, O. Sato, Y. Inagaki, A. Nomura, Y. Tsujii, S. Kang, T. Fukuda and J. Watanabe, *Jpn. J. Appl. Phys.*, 50, 071701 (2011)
5 F. Menoto, I. Nishiyama, Y. Takanishi, and J. Yamamoto, *Soft Matter*, 8, 11526 (2012)
6 P. Oswald, *Eur. Phys. Lett.*, 107, 26003 (2014)
7 O. Sato, T. Kasai, M. Sato, K. Sakajiri, Y. Tsujii, S. Kang, J. Watanabe and M. Tokita, *J. Mater. Chem. C*, 1, 7992 (2013)
8 T. Araki and J. Nagura, *Phys. Rev. E*, 95, 012706 (2017)
9 A. Malevanets and R. Kapral, *J. Chem. Phys.*, 110, 8605 (1999)
10 G. Gompper, T. Ihle, D.M. Kroll, and R.G. Winkler, *Adv. Polym. Sci.*, 110, 8605 (2008)
11 A. Malevanets and R. Kapral, *J. Chem. Phys.*, 112, 7260 (2000)
12 J. T. Padding and A. A. Louis, *Phys. Rev. Lett.*, 93, 220601 (2004)
13 M. Hecht, J. Harting, M. Bier, J Reinshagen, and H. J. Herrmann, *Phys. Rev. E*, 74, 021403 (2006)
14 K. Mussawisade, M. Ripoll, R. G. Winkler and G. Gompper, *J. Chem. Phys.*, 123, 144905 (2005)
15 M. Ripoll, R.G. Winkler and G. Gompper, *G. Eur. Phys. J. E*, 23, 349 (2007)
16 K.-W. Lee and M. G. Mazza, *J. Chem. Phys.*, 142, 164110 (2015)
17 K.-W. Lee and T. Pöschel, *Soft Matter*, 13, 8816 (2017)
18 K. Katayama, D. Kato, K. Nagasaka, M. Miyagawa, W. Y. Sohn and K.-W. Lee , *Sci. Rep.*, 9, 5754 (2019)
19 T. Qian and P. Sheng, *Phys. Rev. E*, 58, 7475 (1998)
20 H. Wu, X. Xu, and C. Liu, *Arch. Ration. Mech. Anal.*, 208, 59-107 (2013)
21 O. Parodi, *J. Phys. (Paris)*, 31, 581 (1970)
22 T. Ihle and D. M. Kroll, *Phys. Rev. E*, 67, 066706 (2003)
23 P. A. Lebwohl and G. Lasher, *Phys. Rev. A*, 6, 426 (1972)
24 H. Kneppe, and F. Schneider and N. K. Sharma, *J. Chem. Phys.*, 77, 3203 (1982)
25 T. Sato and K. Katayama, *Sci. Rep.*, 7, 44801 (2017)

Dynamics Control of In-Plane-Switching Liquid Crystal Cell using Heterogeneous Substrates

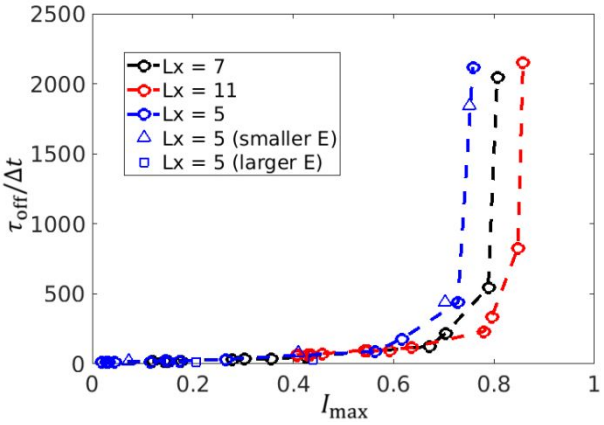

Cell-depth dependent master curves are found in the transmittance/recovery phase space, for a IPS-LCD configuration using heterogeneous substrates.